Analytical Prediction of Iron Core Losses in Flux-Modulated Permanent-Magnet Synchronous Machines

Zakarya Djelloul-Khedda[1*], Kamel Boughrara[2], Frédéric Dubas[3], Abdelhamid Kechroud[4] and Abdelouahab Tikellaline[1]

[1]LESI Laboratory, Univ. Djilali Bounaama Khemis Miliana, Road of Theniet El-had, Khemis Miliana, 44225, Algeria
[2]Ecole Nationale Polytechnique (LRE-ENP), Algiers, 10, av. Pasteur, El Harrach, BP182, 16200, Algeria
[3]Département ENERGIE, FEMTO-ST, CNRS, Univ. Bourgogne Franche-Comté, F90000 Belfort, France
[4]Vanderlande industries Vanderlandelaan, 25466 RB Veghel, Netherlands

In this paper, an analytical approach allowing the prediction of the iron core losses in flux-modulated permanent-magnet synchronous machines (FM-PMSMs). According to the Maxwell-Fourier method (viz., the multi-layer model) and Cauchy's product theorem, the magnetic field distribution is determined in different parts of machine by considering the iron permeability on the basis of the solving both Poisson's and Laplace's equations. Next to the direct current (DC) bias flux density and the minor hysteresis loops, which are taken into account, the Bertotti's model and the flux variation locus (FVL) are employed to calculate the iron core losses under load and no-load conditions in post-processing from the magnetic field analytical calculation. Finally, in order to validate the proposed analytical method, the results are verified by the comparison with finite-element method (FEM). The comparisons show good results of the proposed model.

***Index Terms*— Convolution theorem, flux-modulated permanent-magnet synchronous machines, iron core losses, DC bias, hysteresis loop, flux variation locus, Maxwell-Fourier method, numerical.**

I. Introduction

THE flux-modulated permanent-magnet (PM) synchronous machine (FM-PMSM) is one of the many type of magnetic geared machines, is typically used for wind power systems, because it could provide high-torque applications at low-speed and also characterized by a direct-drive electrical machine without employing the mechanical gearbox [**1**]-[**3**].

However, the existence of the flux-modulation layer in the FM-PMSM, augments not only the fundamental wave but also many high-frequency harmonics field and meanwhile a large harmonic iron losses **[4]**. Therefore, in order to compute the iron losses, the detailed knowledge of the magnetic field distribution in the iron part of this machine is very important.

The finite-element method (FEM) is a powerful tool used for calculate both the spatial and temporal variations of the magnetic flux density and consequently can be analyze the iron losses of electrical machines **[5]**-[**6**]. Generally, the iron loss calculation is based on the loss decomposition approach (i.e., hysteresis/eddy-current/excess losses) [**7**] which can be implemented in the post-processing step of the FEM. Huang *et al.* (2012) **[8]** calculated the core iron losses of PMSM with flux variation locus (FVL) and FEM. The result give a good agreement with the experimental ones without the use of any correction factor. The influence of direct current (DC) bias flux density has been taken into consideration by Simão *et al.* (2009) [**9**] to calculate the iron core losses under DC magnetic bias, where the classical Steinmetz equation has been improved. Zhang *et al.* (2017) **[10]** focused to use the Fourier analysis to predict the iron losses in switched reluctance machine. Usually, the iron losses are computed by FEM from the magnetic field associated to each element in the mesh. However, Chen *et al.* (2017) [**11**] divided the core of the motor in different parts representative points are used to fast iron loss calculation and different modified factors are applied to take into account the losses due to minor loops. The temperature impact in the iron losses under different flux densities, frequencies, and DC bias flux density are investigated by Xue *et al.* (2017) **[12]**, where the improved iron loss model obtained by FEM have been validated by tests on a steel lamination as well as an electrical machine.

Nevertheless, the FEM can provide high precision of iron losses it consumes large computation time. In other hand, the motor designers like better a more fast method. The analytical models deliver the solution to this problem, because they are distinguished by the quick time saving. Many publications have dealt with the iron loss calculations by different analytical models. Sheikh-Ghalavand *et al.* (2010) **[13]** and Tariq *et al.* (2017) **[14]** developed a magnetic equivalent circuit (MEC) to calculate these losses in linear and interior PMSMs, respectively. Messal *et al.* (2017) **[15]** proposed an original approach of iron loss prediction exploiting the dynamic hysteresis model and the magnetic flux density waveforms resulting from generalized nonlinear adaptive MEC using a mesh-based formulation. Tian *et al.* (2017) **[16]** used the complex relative air-gap permeance in surface-mounted PMSMs to estimate the iron losses by using the modified Steinmetz equation. Liang *et al.* (2018) **[17]** used an analytical approach based on the subdomain technique for the prediction of no-load stator iron losses in spoke-type PMSMs. The iron parts are considered to be infinitely permeable, so that the saturation effect is neglected. Nevertheless, the influence of bridge saturation has been considered by using a nonlinear simple MEC. The average magnetic densities of the tooth and yoke for the iron loss evaluation have been obtained on the basis of the continuity of magnetic flux in the air-gap. Desvaux *et al.* (2017) **[18]** used a hybrid method between the subdomain technique and the discretized linear MEC in the pole piece (i.e., modulation layer) for the optimization of coaxial magnetic gear. This enabled them to calculate the magnetic flux density distribution and the

*Corresponding author: Z. Djelloul-Khedda (email: zakaryadoc@hotmail.com).

iron losses in ferromagnetic parts (i.e., internal/external yoke and pole pieces).

Recently, new semi-analytical contributions are developed to take into account the solution of the magnetic field distribution in the iron part. Spranger *et al.* (2016) **[19]** developed a first work based on the Maxwell-Fourier method (viz., the multi-layer model) using the convolution theorem (i.e., Cauchy's product theorem) to determine the solution of the magnetic field distribution in iron parts. The adjacent regions (e.g., rotor or/and stator slots/teeth) are assumed to be one homogeneous region with a relative permeability developed as a Fourier series expansion. This method are used in different machines, viz.: switched reluctance machine **[20]**, synchronous reluctance machine [**21]**, and PMSMs **[22]-[23]**. Meanwhile, Dubas *et al.* (2017) [**24]-[25]** developed a first exact subdomain technique in polar and Cartesian coordinates considering finite soft-magnetic material permeability, which has been applied to an air- or air-cored coil supplied by a constant current. The subdomains connection is performed directly in both directions. The general solutions of Maxwell's equations are deduced by applying the principle of superposition. Recently, this novel scientific contribution has been implemented for radial-flux electrical machines **[26]**. For the same reason, another technique based on subdomain technique and Taylor polynomial has been applied in spoke-type PMSMs **[27]**.

The infinitely permeable assumption in the iron parts used in the various models that are based on the Maxwell-Fourier method does not give the solution of the magnetic field in these parts of iron, which make the iron core loss calculation be indirect from the continuity of magnetic flux in the air-gap and in the slots. Because of that, the rate of error in the calculation is significant **[16]-[17]**. In other hand, the directly calculation of iron core losses have been done successfully in **[22]-[23]** by divided the stator into different segments. However, the stator division procedure in different segments have been done only in the tangential direction and the iron core losses are calculated with negligent both of the iron losses in the rotor part, the DC bias flux density and the minor hysteresis loops, which make the calculation of the iron core losses relatively inaccurate. Moreover, the losses have been obtained at no-load condition and only for one rotor speed. Therefore, the accuracy of analytical model for the calculation of this losses type have not well explained for this different condition.

In this paper, a new analytical model of FM-PMSM is developed for the iron core loss computation with different rotor speed and in both conditions (i.e., no-load and on-load of armature reaction field), the DC bias flux density and the minor hysteresis loops have been taken into account. The developed analytical model is based on the Maxwell-Fourier method (viz. the multi-layer model) and Cauchy's product theorem. The magnetic field distribution in all regions of FM-PMSM are predicted. The iron core losses are calculated by divided the core of the machine in different parts (i.e., in radial and tangential direction) and by used FVL method and Bertotti's model. Finally, all the results from the proposed analytical model are validated by the FEM **[28]**.

II. Motor Configuration

The topology of the studied FM-PMSM with two air-gap is given in **[3]** and is shown in **Fig. 1**. It includes: i) an inner stator with Q_s =12 slots and three-phases (q =3) non-overlapping winding with all teeth wound (viz., the double-layer concentrated winding distribution), which give $p_s = Q_s/q = 4$ stator pole-pair number, and ii) an outer rotor PMs surface-mounted by radially magnetized patterns with p =17 rotor pole-pair number.

For the modulation layer, there are $Q_n = p + p_s = 21$ pole pieces placed between the stator and the rotor. The gear ratio $G_r = -p/p_s = -4.25$. The relation between the stator rotary field frequency f_e and the machine mechanical rotation frequency F is $F = f_e/G_r$ with $f_e = f_{el}/p_s$ where f_{el} is the electrical frequency. In order to get 50 Hz currents in the stator armature, then the stator rotary field frequency will be f_e = 12.5 Hz (i.e., 750 rpm). Therefore, the outer-rotor frequency it must be to 2.94 Hz (i.e., 176 rpm) in the opposite direction.

However, in the configuration presented in **Fig. 1**, the stator winding is placed in the clockwise direction and the rotor is rotated in the anti-clockwise direction. Thus, we are take the value absolute of the gear ratio $|G_r|$ during the calculations procedures (i.e., the indication of the rotation direction are taken physically not mathematically).

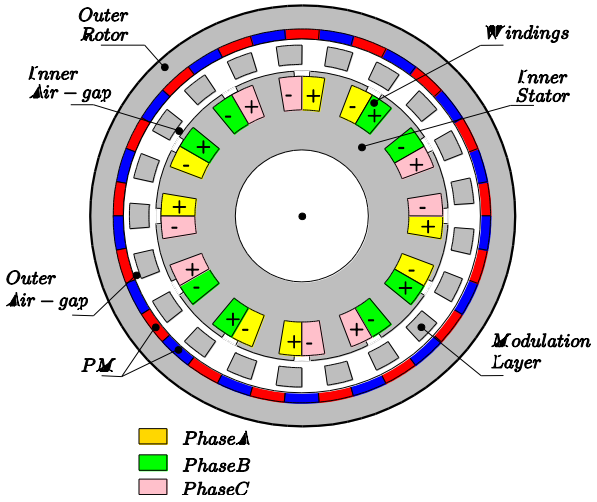

Fig. 1. Configuration of the studied FM-PMSM.

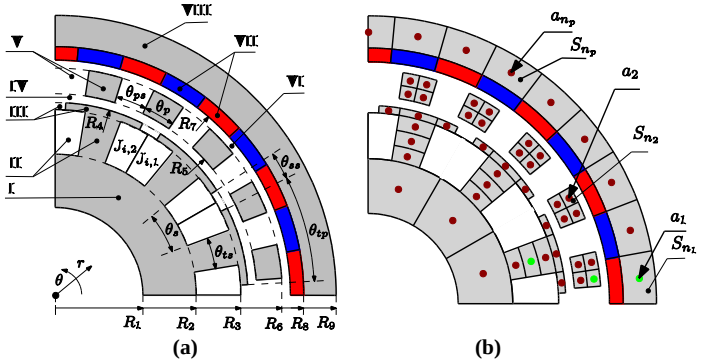

Fig. 2. Studied FM-PMSM **(a)** Simplified model and **(b)** Different areas and feature points for magnetic flux density and iron loss calculation.

III. Problem Formulation Assumptions

The model is subedit in two-dimensional polar coordinate system and has been partitioned into 8 regions as shown on **Fig. 2(a)**. Region I and VIII represented the stator and rotor yoke respectively, Region II represented the stator slots and teeth, Region III represented the stator isthmus-opening and tooth-tips, Region IV and VI are represented the inner and outer air-gap respectively, Region V represented the modulation layer, and Region VII represented the PMs. During each region, the magnetic field is assumed periodic. The model is formulated in magnetic vector potential with the following assumptions:

- The magnetic materials are considered as isotropic with constant magnetic permeability corresponding to linear zone of the *B(H)* curve;
- All electrical conductivities of materials are supposed as nulls (i.e., the eddy-current reaction field in the materials are neglected);
- The stator slots/teeth have radial sides;
- The end-effects are neglected.

The angular position of the $i_n{}^{\text{th}}$ modulation layer elements (i.e., Region V) and $i_s{}^{\text{th}}$ stator elements (i.e., Region II and Region III) are defined respectively by

$$\alpha_{i_s}^{s} = \frac{2\pi}{Q_s}(i_s - 1) \tag{1}$$

$$\alpha_{i_n}^{n} = \frac{2\pi}{Q_n}(i_n - 1) \tag{2}$$

IV. Analytical Model

Magnetic field calculation in all regions is calculated from by solving the following Laplace's and Poisson's matrix equations

$$\frac{\partial^2 \mathbf{A}_z^k|_r}{\partial r^2} + \frac{1}{r}\frac{\partial \mathbf{A}_z^k|_r}{\partial r} - \left(\frac{\mathbf{V}^k}{r}\right)^2 \mathbf{A}_z^k|_r = \begin{cases} 0, & k = I, III, IV, V, VI \text{ and } VIII \\ -\boldsymbol{\mu}_c^k \mathbf{J}_z^k, & k = II \\ -j\dfrac{\mu_0}{r}\mathbf{N}\,\mathbf{M}_r^k, & k = VII \end{cases} \tag{3}$$

where

$$\mathbf{N} = \mathrm{diag}[-N \cdots N] \tag{4}$$

$$\mathbf{V}^k = \begin{cases} \mathbf{N}, & k = I, IV, VI, VII \text{ and } VIII \\ \left(\boldsymbol{\mu}_c^k \mathbf{N}\, \boldsymbol{\mu}_{c,inv}^k \mathbf{N}\right)^{\frac{1}{2}}, & k = II, III \text{ and } V \end{cases} \tag{5}$$

$$\mathbf{M}_r = \mathrm{diag}\left(\left[\widehat{M}_{r_{-N}} \cdots \widehat{M}_{r_N}\right]^T\right).e^{-j\mathbf{N}\delta} \tag{6}$$

$$\widehat{M}_{r_n} = \begin{cases} \dfrac{2pB_{rem}}{n\pi\mu_0}\sin\left(\dfrac{n\pi}{2p}\right), & n \neq 0 \\ 0, & n = 0 \end{cases} \tag{7}$$

$$\mathbf{J}_z = \left[\hat{J}_{z,-N} \quad \cdots \quad \hat{J}_{z,N}\right]^T \tag{8}$$

$$\hat{J}_{z,n} = \begin{cases} \displaystyle\sum_{i=1}^{Qs} \frac{1}{2\pi j n}\left[J_{i,1}\, e^{-jn\frac{\theta_s}{2}}\left(e^{jn\frac{\theta_s}{2}} - 1\right) \right. \\ \left. \quad + J_{i,2}\, e^{jn\frac{\theta_s}{2}}\left(1 - e^{-jn\frac{\theta_s}{2}}\right)\right] e^{jn\alpha_{i_s}^{s}} & n \neq 0 \\ 0 & n = 0 \end{cases} \tag{9}$$

where $j = \sqrt{-1}$; $n = 1,2 \ldots N$ is spatial harmonic orders; $J_{i,1}$ & $J_{i,2}$ are the stator current densities of slots for two tangential parts for three-phases current are given in **Appendix**.

Using the separation of variables method in r and θ, the general solution of **(3)** for each regions are formulated as

$$\mathbf{A}_z^I|_r = \left(\frac{r}{R_2}\right)^{\boldsymbol{\lambda}^I} \mathbf{a}^I + \left(\frac{R_1}{r}\right)^{\boldsymbol{\lambda}^I} \mathbf{b}^I \tag{10}$$

$$\mathbf{A}_z^{II}|_r = \mathbf{W}^{II}\left(\frac{r}{R_3}\right)^{\boldsymbol{\lambda}^{II}} \mathbf{a}^{II} + \mathbf{W}^{II}\left(\frac{R_2}{r}\right)^{\boldsymbol{\lambda}^{II}} \mathbf{b}^{II} + \left[\mathbf{V}^{II\,2} - 4\mathbf{I}\right]^{-1} \boldsymbol{\mu}_c^{II}\,\mathbf{J}_z \tag{11}$$

$$\mathbf{A}_z^{III}|_r = \mathbf{W}^{III}\left(\frac{r}{R_4}\right)^{\boldsymbol{\lambda}^{III}} \mathbf{a}^{III} + \mathbf{W}^{III}\left(\frac{R_3}{r}\right)^{\boldsymbol{\lambda}^{III}} \mathbf{b}^{III} \tag{12}$$

$$\mathbf{A}_z^{IV}|_r = \left(\frac{r}{R_5}\right)^{\boldsymbol{\lambda}^{IV}} \mathbf{a}^{IV} + \left(\frac{R_4}{r}\right)^{\boldsymbol{\lambda}^{IV}} \mathbf{b}^{IV} \tag{13}$$

$$\mathbf{A}_z^{V}|_r = \left(\frac{r}{R_6}\right)^{\boldsymbol{\lambda}^{V}} \mathbf{a}^{V} + \left(\frac{R_5}{r}\right)^{\boldsymbol{\lambda}^{V}} \mathbf{b}^{V} \tag{14}$$

$$\mathbf{A}_z^{VI}|_r = \left(\frac{r}{R_7}\right)^{\boldsymbol{\lambda}^{VI}} \mathbf{a}^{VI} + \left(\frac{R_6}{r}\right)^{\boldsymbol{\lambda}^{VI}} \mathbf{b}^{VI} \tag{15}$$

$$\mathbf{A}_z^{VII}|_r = \left(\frac{r}{R_8}\right)^{\boldsymbol{\lambda}^{VII}} \mathbf{a}^{VII} + \left(\frac{R_7}{r}\right)^{\boldsymbol{\lambda}^{VII}} \mathbf{b}^{VII} + j\mu_0\left[\mathbf{V}^{VII\,2} - \mathbf{I}\right]^{-1} \mathbf{N}\,\mathbf{M}_r \tag{16}$$

$$\mathbf{A}_z^{VIII}|_r = \left(\frac{r}{R_9}\right)^{\boldsymbol{\lambda}^{VIII}} \mathbf{a}^{VIII} + \left(\frac{R_8}{r}\right)^{\boldsymbol{\lambda}^{VIII}} \mathbf{b}^{VIII} \tag{17}$$

where $\mathbf{a}^k$ & $\mathbf{b}^k$ are the column vectors of the constants unknown coefficients, $\mathbf{W}^k$ is the diagonal eigenvector matrix of $\mathbf{V}^k$, $\boldsymbol{\lambda}^k$ is the diagonal eigenvalue matrix of $\mathbf{V}^k$ if $k = II, III$ and V or $\boldsymbol{\lambda}^k = |\mathbf{N}|$ if $k = I, IV, VI, VII$ and $VIII$, and $\mathbf{I}$ is a diagonal identity matrix with same size as $\mathbf{N}$.

The application of the Dirichlet boundary conditions to the inner boundary of Region I $\left(\mathbf{A}_z^I|_{r=R_1} = 0\right)$ and the outer boundary of Region VIII $\left(\mathbf{A}_z^{VIII}|_{r=R_9} = 0\right)$, **(10)** and **(17)** are reduced to

$$\mathbf{A}_z^I|_r = \left[\left(\frac{r}{R_2}\right)^{\boldsymbol{\lambda}^I} - \left(\frac{R_1}{R_2}\right)^{\boldsymbol{\lambda}^I}\left(\frac{R_1}{r}\right)^{\boldsymbol{\lambda}^I}\right]\mathbf{a}^I \tag{18}$$

$$\mathbf{A}_z^{VIII}|_r = \left[\left(\frac{R_7}{r}\right)^{\boldsymbol{\lambda}^{VIII}} - \left(\frac{R_7}{R_8}\right)^{\boldsymbol{\lambda}^{VIII}}\left(\frac{r}{R_8}\right)^{\boldsymbol{\lambda}^{VIII}}\right]\mathbf{b}^{VIII} \tag{19}$$

The boundary conditions between two adjacent media to be satisfied by **(18)**, **(19)** and **(11)-(16)** are

$$\mathbf{A}_z^{k-1} - \mathbf{A}_z^k|_{r=R_k} = 0 \tag{20}$$

$$\boldsymbol{\mu}_{c,inv}^{k-1}\left(\partial \mathbf{A}_z^{k-1}/\partial r\right) - \boldsymbol{\mu}_{c,inv}^{k}\left(\partial \mathbf{A}_z^{k}/\partial r\right)\big|_{r=R_k} = 0 \tag{21}$$

where k represent the all regions, and $\boldsymbol{\mu}_{c,inv}$ is the convolution matrices of the inverse magnetic permeability in the Region II, III and V given by **[19]** and **[22]**

$$\boldsymbol{\mu}_{c,inv} = \begin{bmatrix} \hat{\mu}_0^{inv} & \cdots & \hat{\mu}_{-2N}^{inv} \\ \vdots & \ddots & \vdots \\ \hat{\mu}_{2N}^{inv} & \cdots & \hat{\mu}_0^{inv} \end{bmatrix} \tag{22}$$

$$\hat{\mu}_n^{inv,k} = \begin{cases} \sum_{i=1}^{Q} \frac{1}{2\pi jn}\left[\frac{1}{\mu_{iron}} e^{-jn\frac{\theta_{sl}^k}{2}}\left(1-e^{-jn\theta_{te}^k}\right) + 2j\frac{1}{\mu_0}\sin\left(\frac{n\theta_{sl}^k}{2}\right)\right] e^{jn\alpha_i}, & n \neq 0 \\ \sum_{i=1}^{Q} \frac{1}{2\pi}\left(\frac{1}{\mu_{iron}}\theta_{te}^k + \frac{1}{\mu_0}\theta_{sl}^k\right), & n = 0 \end{cases} \quad (23)$$

where $\{\theta_{te}, \theta_{sl}, Q, i, \alpha_i\}$ are replaced in the second region by $\{\theta_{ts}, \theta_s, Q_s, i_s, \alpha_{i_s}^s\}$, in the third region by $\{\theta_{tp}, \theta_{ss}, Q_s, i_s, \alpha_{i_s}^s\}$ and in the fifth region by $\{\theta_p, \theta_{ps}, Q_n, i_n, \alpha_{i_n}^n\}$, the naming of this opening angle are given in Table I. In the other regions $\boldsymbol{\mu}_{c,inv} = [\mu_{iron}\mathbf{I}]^{-1}$ for $k = I$ and $VIII$, and $\boldsymbol{\mu}_{c,inv} = [\mu_0\mathbf{I}]^{-1}$ for $k = IV, VI$ and VII.

The system of fourteen $[8_{regions}\text{x}2]$ boundary conditions matrix equations **(20)** and **(21)** could be used to determine the unknown coefficients of magnetic vector potentials in the all regions according to **[20]**. Then, the radial and tangential magnetic flux density B_r and B_θ in the all regions can be deduced from the magnetic vector potentials matrix by

$$\mathbf{B_r}|_r = -j\frac{1}{r}\,\mathbf{N}\,\mathbf{A}_z|_r \quad (24)$$

$$\mathbf{B}_\theta|_r = -\frac{\partial \mathbf{A}_z|_r}{\partial r} \quad (25)$$

The radial and tangential magnetic flux density $\{B_r;\ B_\theta\}$ are calculated with one point by

$$B_r(r,\theta) = \Re e\left([\mathbf{B_r}|_r]^T.\left[e^{-j\bar{\mathbf{N}}\theta}\right]^T\right) \quad (26)$$

$$B_\theta(r,\theta) = \Re e\left([\mathbf{B}_\theta|_r]^T.\left[e^{-j\bar{\mathbf{N}}\theta}\right]^T\right) \quad (27)$$

where

$$\bar{\mathbf{N}} = [-N \cdots N] \quad (28)$$

and with N_s points in the tangential direction by

$$B_r\left(r,\theta_{N_s}\right) = \Re e([\mathbf{B_r}|_r]^T.e^{-j\mathbf{N}_\theta}) \quad (29)$$

$$B_\theta\left(r,\theta_{N_s}\right) = \Re e([\mathbf{B}_\theta|_r]^T.e^{-j\mathbf{N}_\theta}) \quad (30)$$

where

$$\mathbf{N}_\theta = \text{repmat}[-\boldsymbol{\theta}, 2N+1] \quad (31)$$

$$\boldsymbol{\theta} = \left[\theta_1, \theta_2 \cdots \theta_{N_s}\right] \quad (32)$$

$$\text{repmat}[-\boldsymbol{\theta}, 2N+1] = \begin{bmatrix} -\theta_1 & -\theta_2 & \cdots & -\theta_{N_s} \\ -\theta_1 & -\theta_2 & \cdots & -\theta_{N_s} \\ \vdots & \vdots & \vdots & \vdots \\ -\theta_1 & -\theta_2 & \cdots & -\theta_{N_s} \end{bmatrix} \begin{matrix} 1 \\ 2 \\ \vdots \\ 2N+1 \end{matrix} \quad (33)$$

$$\begin{cases} \theta_1 = 0\ (rad) \\ \theta_2 = \theta_1 + \Delta\theta \\ \theta_{N_s} = 2\pi\ (rad) \\ \Delta\theta = \theta_{N_s}/(N_s - 1) \end{cases} \quad (34)$$

V. Validation of Magnetic Field Distribution by the FEM

To verify the validity of the proposed model, the spatial variations of magnetic flux densities (i.e., radial and tangential components of magnetic field distribution) in the inner and outer air-gap as well as the temporal variations of magnetic flux densities at three different points (green color in **Fig. 2(b)**) calculated with the analytical model are compared with those obtained from the FEM. The main parameters of the FM-PMSM can be found in **Table I**.

A. Comparison of Spatial Magnetic Field Distribution

Magnetic flux density waveforms in the inner and outer air-gap are shown in **Fig. 3** and **Fig. 4**, which are the function of the tangential position θ, for no-load and on-load condition, respectively (i.e., with only PM and with both PM and armature reaction field) through $I_a = \hat{I}\sin(0)$, $I_b = \hat{I}\sin(-2\pi/3)$ and $I_c = \hat{I}\sin(2\pi/3)$ where $\hat{I} = 16\ A$.

The computation time required for the magnetic field calculation in linear analytical model and FEM (linear and nonlinear) of FM-PMSM in one rotor position are shown in **Table II**. In linear analytical model, the resulting system of equations has 1,608 and 2,408 unknown coefficients for N = 100 and N = 150 respectively. The linear and nonlinear FEM for 6,380 boundary and 119,108 elements of first order.

TABLE I
MAIN PARAMETERS OF FM-PMSM.

Symbols	Parameters	Values (Units)
B_{rem}	PMs remanence flux density	1.2 (T)
μ_{rm}	PMs relative permeability	1
Q_s	Number of stator slots	12
p	Number of pole-pairs	17
Q_n	Number of modulation layer	21
N_c	Conductor number of slot coil	72
w_r	Rotor speed	18.47 (rad/s)
R_1	Shaft Radius	45 (mm)
R_2	Inner radius of the slot	70 (mm)
R_3	Inner radius of the slot-openings	90 (mm)
R_4	Radius of the stator surface	93 (mm)
R_5	Inner radius of the modulation layer	94 (mm)
R_6	Outer radius of the modulation layer	104 (mm)
R_7	Inner radius of the PMs	105 (mm)
R_8	Rotor bore radius	111 (mm)
R_9	Radius of the external rotor surface	125 (mm)
L_u	Stack length	100 (mm)
θ_s	Stator slot angle	$1.25(\pi/Q_s)$ (rad)
θ_{ts}	Stator teeth opening angle	$(2\pi/Q_s) - \theta_s$ (rad)
θ_{ss}	Stator slot opening angle	$(1/3)\theta_s$ (rad)
θ_{tp}	Stator teeth tips opening angle	$(2\pi/Q_s) - \theta_{ss}$ (rad)
θ_{ps}	Modulation layer slot opening angle	π/Q_n (rad)
θ_p	Modulation layer opening angle	$(2\pi/Q_n) - \theta_{ps}$ (rad)

TABLE II
COMPUTATION TIMES.

	Linear Analytical Model		FEM	
	N=100	N=150	Linear	Nonlinear
Time [sec]	2.71	7.54	16	57

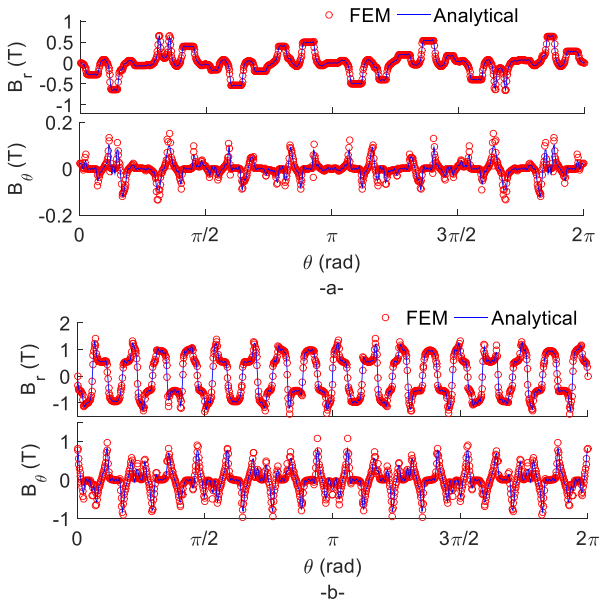

Fig. 3. Radial and tangential magnetic flux density of FM-PMSM at no-load condition in the middle of the **(a)** inner air-gap, and **(b)** outer air-gap.

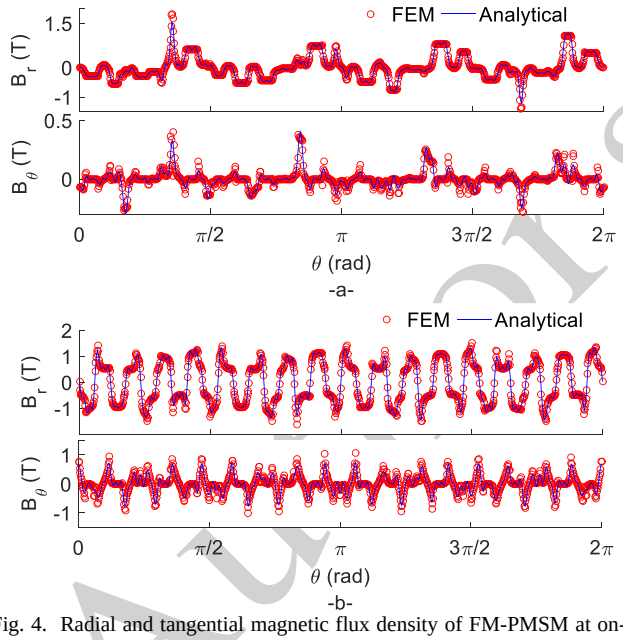

Fig. 4. Radial and tangential magnetic flux density of FM-PMSM at on-load condition in the middle of the **(a)** inner air-gap, and **(b)** outer air-gap.

For $N_s = 500$ points and using $N = 100$ spatial harmonics, the resulting system of equations has $[(2N+1).8_{regions}]$ unknown coefficients. **Fig. 5** shows another presentation of the magnetic field distribution in all machines regions where the magnitude of **B** is plotted. It is observed that the analytical model has excellent similar accuracy to the FEM. Instead of the iron core relative permeability value that are used in the other results ($\mu_{r,iron} = 4{,}000$), **Fig. 6** shows the capability of the model to give good results of two different values of the iron core relative permeability (100 and 4,000). The saturation effect appears clearly in the results of the radial and tangential component of the magnetic flux density in the inner air-gap [see **Fig. 6(a)** and **6(b)**]. However, in **Fig. 6(c)** and **6(d)** the saturation effects are less in the outer air-gap region, due to proximity of this region to the PM region. The comparison between the linear analytical model and the nonlinear FEM is illustrated in **Fig. 7**, where the radial magnetic flux density in the inner and outer air-gap has been presented under load condition. The resultants show a strong convergence between the two models. This is because the type of studied machine which is working at the linear part of *B(H)* curve.

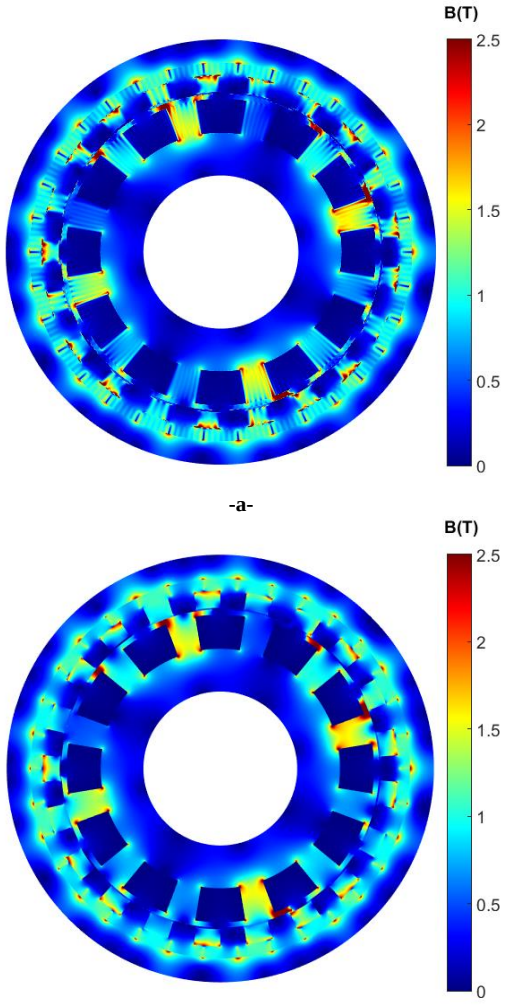

Fig. 5. Magnetic flux density level of FM-PMSM for on-load condition $\hat{I}$ = 16 A: **(a)** Analytical, and **(b)** FEM.

B. Comparison of Temporal Magnetic Field Variations at Three Different Points in Stator, Modulation layer and Rotor

In the both conditions (i.e., no-load and on-load of armature reaction field), the radial and tangential magnetic flux density waveform in the stator of the proposed method [see **Fig. 8** and **Fig. 9**] have similar shape with that of FEM, can also be observed in the loci shown in **Fig. 10** and **Fig. 11**.

For the modulation layer, in the **Fig. 8(b)** and **Fig. 9(b)** the comparison shows analytical and FEM waveforms of the radial and tangential magnetic flux density matches very well except little phase shift in the tangential component can be well observed in the **Fig. 10(b)** and **Fig. 11(b)**, because the Gibbs' phenomenon contributes to the error. The same problem have bas been observed before by Liang *et al.* [**17**]. However, the influence of the tangential magnetic flux density on the iron losses is much smaller than the radial component.

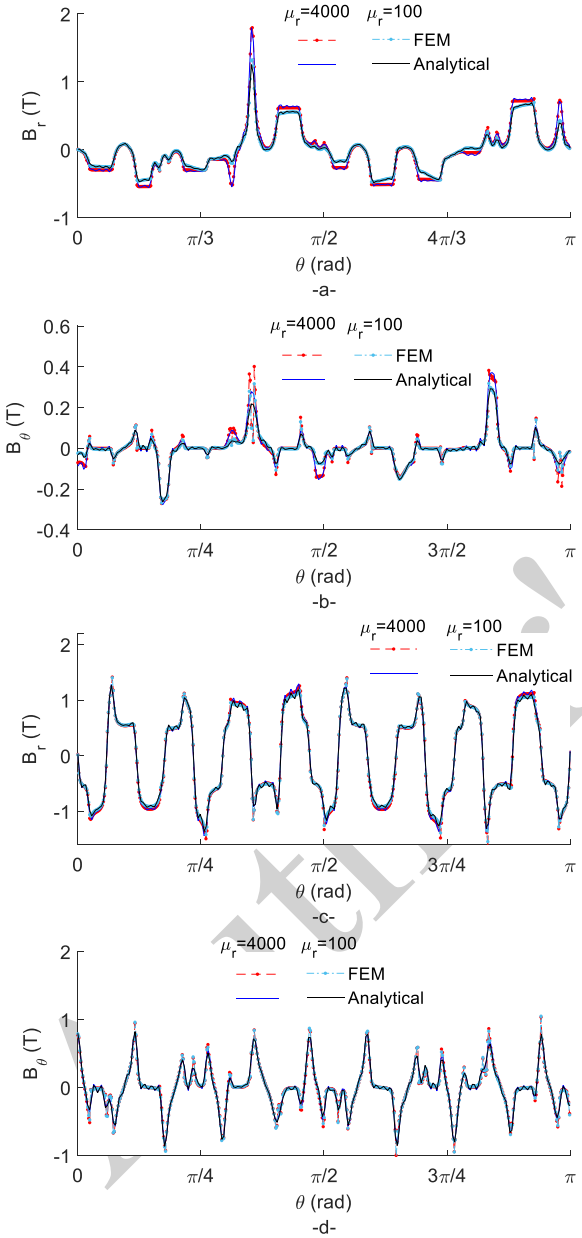

Fig. 6. Magnetic flux density of FM-PMSM with two different permeability values at on-load condition in the middle of the inner air-gap **(a)** radial and **(b)** tangential component and in the middle of the outer air-gap **(c)** radial and **(d)** tangential component.

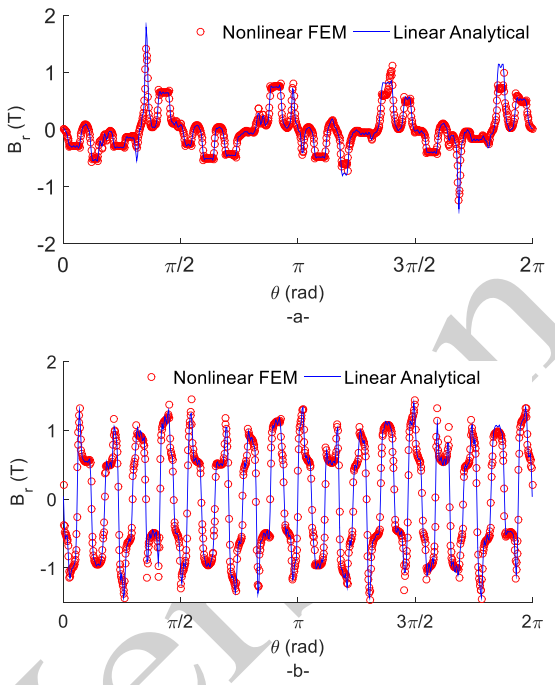

Fig. 7. Radial magnetic flux density of FM-PMSM with linear analytical model and nonlinear FEM at on-load condition in the middle of the **(a)** inner air-gap, and **(b)** outer air-gap.

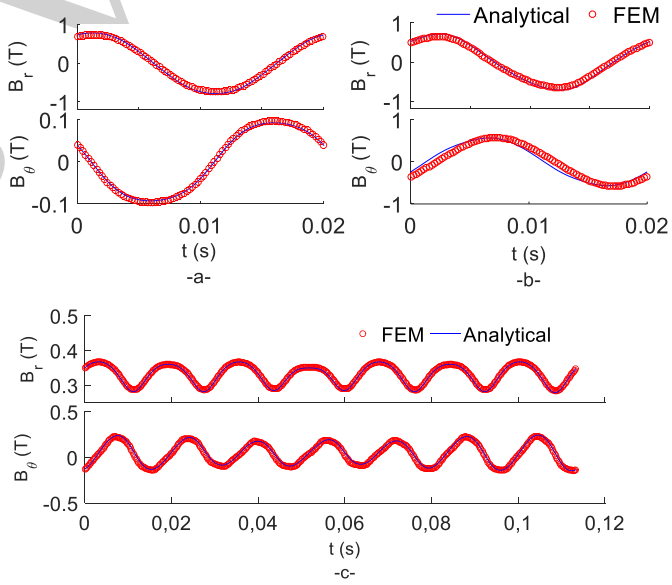

Fig. 8. No-load evolution in the radial and tangential components of magnetic flux density for a point on the: **(a)** stator, **(b)** modulation layer, and **(c)** rotor.

Fig. 10(c) and **Fig. 11(c)** show the waveforms and loci comparison of the results in the rotor, respectively, the analytical and FEM waveforms of the both radial and tangential magnetic flux density are identical withe different frequency to the other results in the fixed element (i.e., stator and modulation layer). We can see the exist of the dc bias flux density in radial component. This is because the presence of PM in the rotor part. Nevertheless, the magnetic flux density values are small compared to the other values in the other part of the machine.

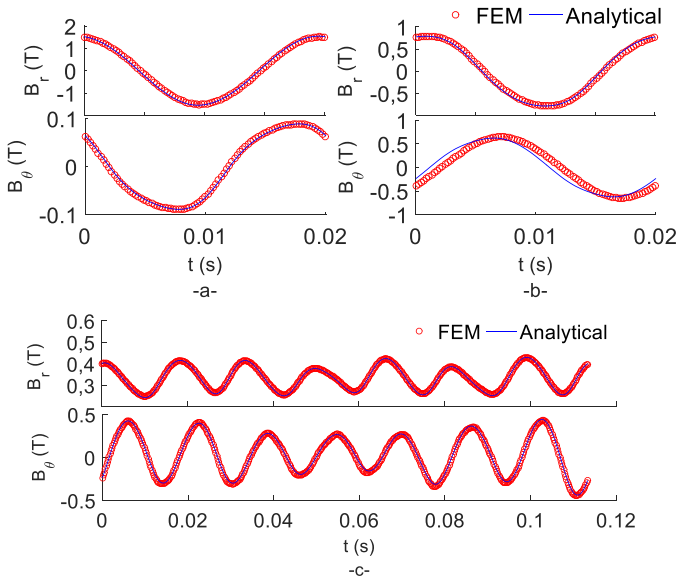

Fig. 9. On-load evolution in the radial and tangential components of magnetic flux density for a point on the: **(a)** stator, **(b)** modulation layer, and **(c)** rotor.

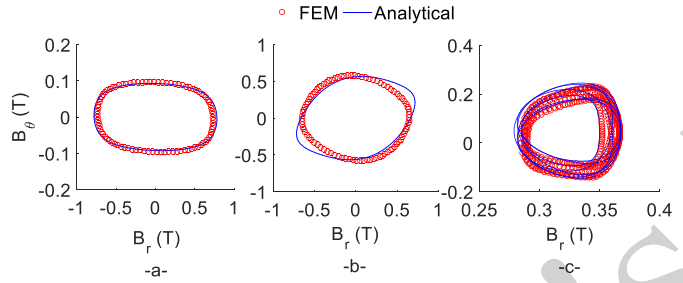

Fig. 10. Loci of magnetic flux density at no-load condition for a point on the: **(a)** stator, **(b)** modulation layer, and **(c)** rotor.

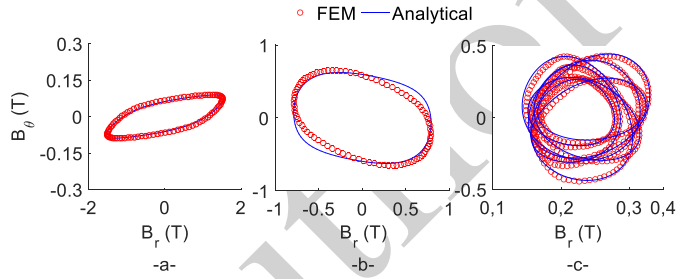

Fig. 11. Loci of magnetic flux density at on-load condition for a point on the: **(a)** stator, **(b)** modulation layer, and **(c)** rotor.

VI. Iron Loss Computation

For a no-sinusoidal excitation, the calculation of iron core losses P_{iron} in the FM-PMSM is defined by the Bertotti's model expressed in three contributions **[7]**, taking into account the influence of minor hysteresis loops **[30]** and the DC bias flux density **[9]**. The iron core losses is expressed by:

$$\begin{aligned} P_{iron} &= P_{hys} + P_{edd} + P_{ex} \\ &= k_{hys}.f(B_m)^{\alpha}.C_f.\varepsilon(B_{dc}) \\ &\quad + \frac{\sigma d_l f}{12}\int_0^T \left(\frac{dB(t)}{dt}\right)^2 dt \\ &\quad + k_{ex} f \int_0^T \left|\frac{dB(t)}{dt}\right|^{1.5} dt \end{aligned} \tag{35}$$

where P_{hys}, P_{edd}, and P_{ex} are respectively the hysteresis, eddy-current and excess losses; B is the iron core magnetic density; B_m is the peak value of the magnetic flux density in the iron core; $T = 1/f$ is the iron core magnetic flux density period with f the frequency; k_{hys}, k_{ex} and $\alpha = 2$ are respectively the coefficient of hysteresis losses, excess losses and the Steinmetz constant; σ is the electrical conductivity; and d_l is the lamination thickness. The correction factor C_f used to take the total loss depend on the magnitude of every local minor loops is given by

$$C_f = 1 + \frac{k}{B_m}\sum_{i=1}^{n_i} \Delta B_i \tag{37}$$

where k a coefficient in the range 0.6 to 0.7, n_i is the number of minor loops and ΔB_i is the magnitude of i^{th} minor loop are calculated by working on all the local maximum and minimum points in the flux density waveforms [see **Fig. 18**].

The correction factor $\varepsilon(B_{dc})$ used to take the influence of dc bias flux density [see **Fig. 18(b)**] is defined as

$$\varepsilon(B_{dc}) = 1 + k_{dc}\, B_{dc}^{\alpha_{dc}} \tag{38}$$

where B_{dc} is the DC bias flux density, k_{dc} and α_{dc} are the DC bias coefficients and can be obtained by fitting the measured results.

A. Flux Variation Locus Method

Because the iron core loss is affected not only by the alternating flux, but also the rotational flux in the FM-PMSM. It is useful to use the FVL method where the rotational flux effect can also be taken into account **[8]**. **Fig. 12** show the elliptical locus in the rotating machine, where $B_{\parallel}$ and $B_{\perp}$ are respectively the major and minor of magnetic flux density which can be determined from $\{B_r;\ B_\theta\}$ by using **(39)** and the algorithm shown in **Fig. 13**. The angle ϕ are varied from 0° to 180° with a step 0.5°, then $\{B_{\parallel};\ B_{\perp};\gamma\}$ corresponding to $\{B_{r,\phi};\ B_{\theta,\phi};\phi\}$ when $B_{r,\gamma}$ equal the minimum value from the all maximum values $(\hat{B}_{\theta,\phi})$ of $B_{r,\phi}$.

$$\begin{bmatrix} B_{r,\phi}(t) \\ B_{\theta,\phi}(t) \end{bmatrix} = \mathbf{M}^{rot}(\phi) \begin{bmatrix} B_r(t) - B_{r,aver}(t) \\ B_\theta(t) - B_{\theta,aver}(t) \end{bmatrix} \tag{39}$$

$$\mathbf{M}^{rot}(\phi) = \begin{bmatrix} \cos\phi & \sin\phi \\ -\sin\phi & \cos\phi \end{bmatrix} \tag{40}$$

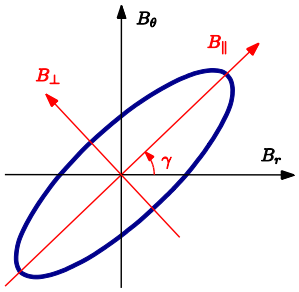

Fig. 12. Elliptical locus for the iron loss evaluation.

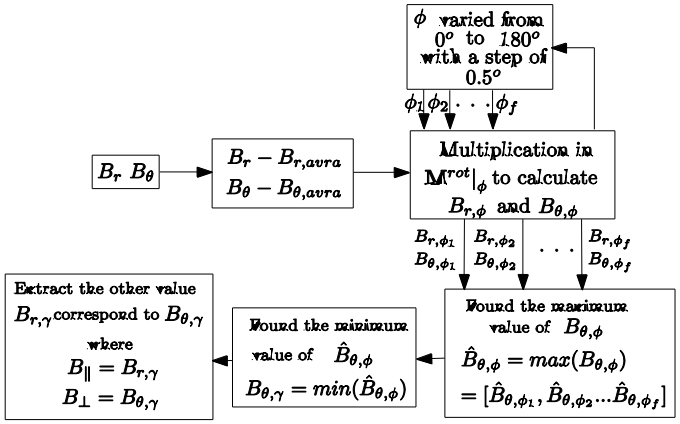

Fig. 13. Diagram to calculate $B_\parallel$ and $B_\perp$.

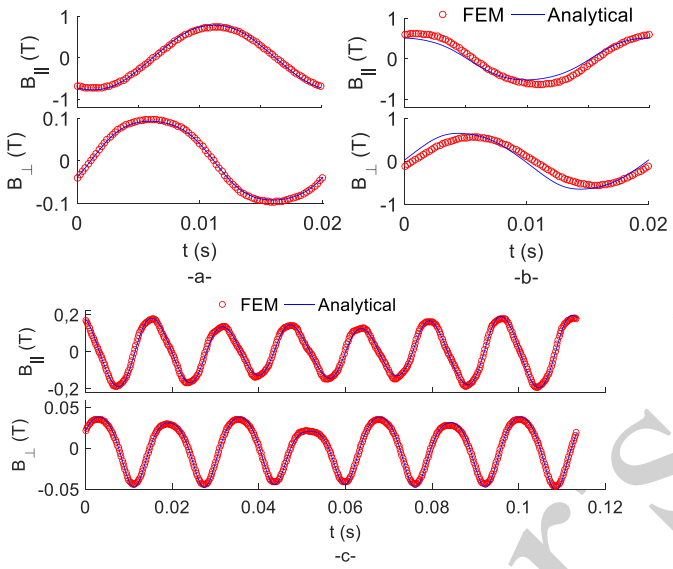

Fig. 14. No-load evolution in the major and minor components of magnetic flux density for a point on the: **(a)** stator, **(b)** modulation layer, and **(c)** rotor.

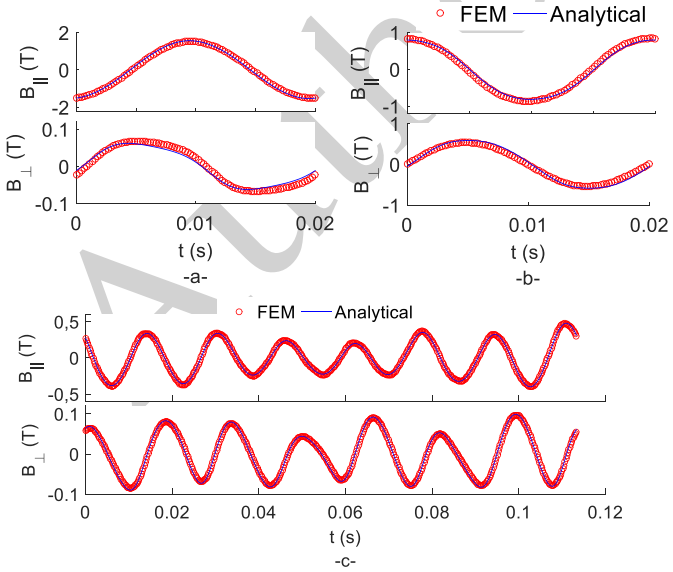

Fig. 15. On-load evolution in the major and minor components of magnetic flux density for a point on the: **(a)** stator, **(b)** modulation layer, and **(c)** rotor.

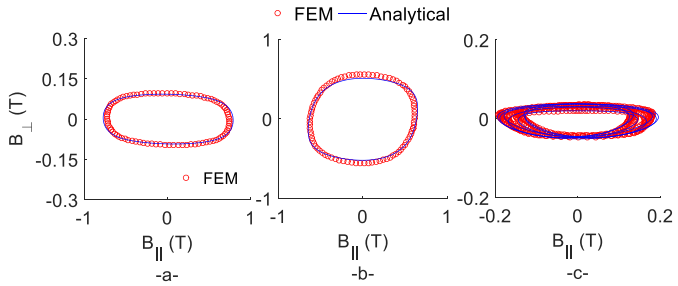

Fig. 16. Loci of magnetic flux density at on-load condition for a point on the: **(a)** stator, **(b)** modulation layer, and **(c)** rotor.

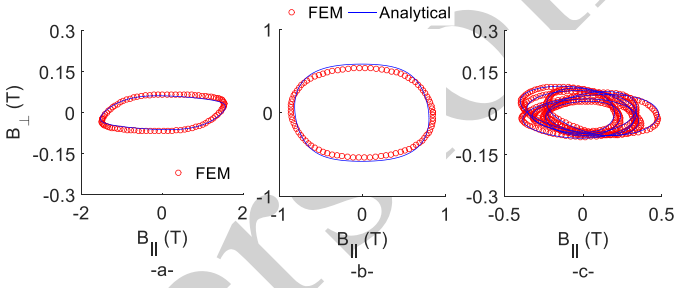

Fig. 17. Loci of magnetic flux density at no-load condition for a point on the: **(a)** stator, **(b)** modulation layer, and **(c)** rotor.

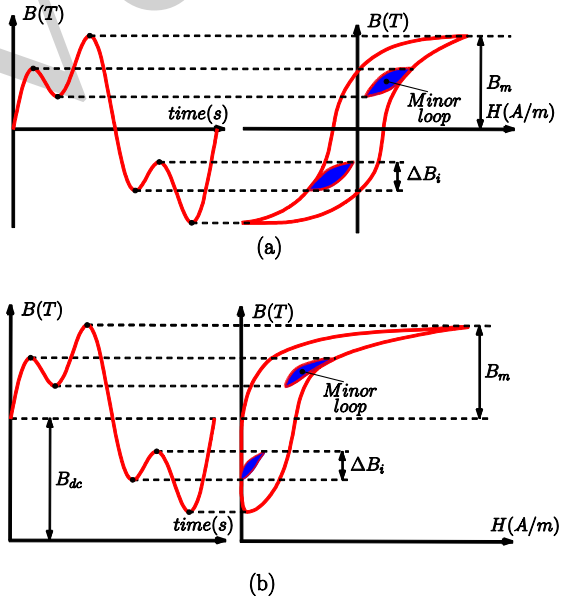

Fig. 18. Hysteresis loop with minor loops **(a)** without DC bias flux density and **(b)** with DC bias flux density.

In **(39)**, the ripples values of $\{B_r;\ B_\theta\}$ are used by subtracted their average values to calculate the iron losses. This case appears in the rotor parte where the average values of $\{B_r\}$ are not null [see **Fig. 8(c)**, **Fig. 9(c)**, **Fig. 10(c)** and **Fig. 11(c)**].

The application of FVL method is carried out by the algorithm presented in **Fig. 13** to the temporal magnetic field variations at three different points in the FM-PMSM presented in **Fig. 8 ~ 11** are shown in **Fig. 14 ~ 17**. The algorithm give a good results in booth models (i.e., analytical and FEM) and the little phase shift in the tangential component which appeared in **Fig. 10(b)** and **Fig. 11(b)** has disappeared [see **Fig. 16(b)** and **Fig. 17(b)**].

TABLE III
IRON LOSS COEFFICIENTS M270-35A

Symbols	Parameters	Values (Units)
k_{hys}	Hysteresis losses coefficient	130.24 (W.s.T$^{-\alpha}$.m^{-3})
k_{ex}	Excess loss coefficient	3.57 E-1 (W.s$^{1.5}$.T$^{-1.5}$.m^{-3})
α	Steinmetz constant	2
σ	Conductivity	1.92 E6 (S.m^{-1})
d_l	Lamination thickness	0.35 (mm)
ρ	Lamination mass density	7.65 E3 (kg.m^{-3})

The iron core losses are calculated by taken into account the rotational flux effect in the FM-PMSM, in different areas S_{n_p} [see **Fig. 2(b)**] where $n_p = 1, 2 \ldots N_p$ from the magnetic flux density in different points a_{n_p} where **(35) ~ (36)** are extended to

$$P_{hys} = k_{hys} V_{n_p} f \left[{B_{r,m}}^{\alpha} . C_{f.r.} . \varepsilon(B_{r.dc}) + {B_{\theta,m}}^{\alpha} . C_{f.\theta} . \varepsilon(B_{\theta.dc}) \right] \quad (41)$$

$$P_{edd} = \frac{\sigma d_l}{12} V_{n_p} f \int_0^T \left[\left(\frac{dB_{\parallel}(t)}{dt} \right)^2 + \left(\frac{dB_{\perp}(t)}{dt} \right)^2 \right] dt \quad (42)$$

$$P_{ex} = k_{ex} V_{n_p} f \int_0^T \left[\left(\frac{dB_{\parallel}(t)}{dt} \right)^2 + \left(\frac{dB_{\perp}(t)}{dt} \right)^2 \right]^{3/4} dt \quad (43)$$

where $V_{n_p} = S_{n_p} L_u$ are the different volume for different iron parts loss calculation, and $B_{\parallel,m}$ & $B_{\perp,m}$ are respectively the peak values of the major and minor magnetic density in the iron core.

VII. VALIDATION OF IRON LOSSES BY THE FEM

Using the coefficients are given in **Table III**, the iron losses are calculated under no-load and on-load condition with three-phases sinusoidal currents where $w = 2\pi f_e$, $\hat{I}$ varied from 0 to 16 A. The rotor speed are varied from the half to seven times of (176 rpm). The Bertotti's model are also used by FEM. **Fig. 19** and **Fig. 20** show the variation of hysteresis, eddy current and excess loss with speed in the no-load and on-load condition, respectively. It is observed that the analytical results are agrees well with the FEM despite a little difference where the analytical results are a little bigger than the FEM one in the high speed.

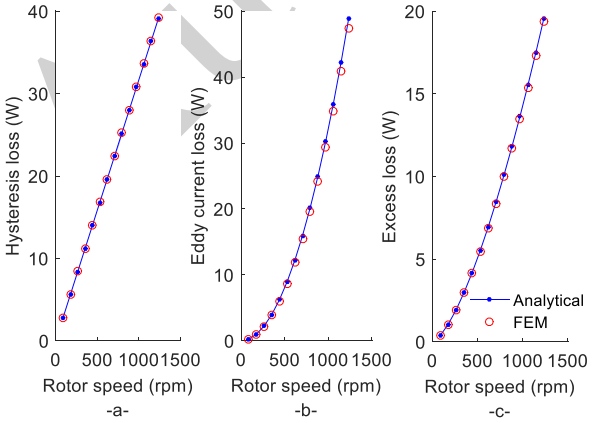

Fig. 19. No-load analytically and FEM predicted iron losses: **(a)** Hysteresis, **(b)** Eddy-current, and **(c)** Excess loss.

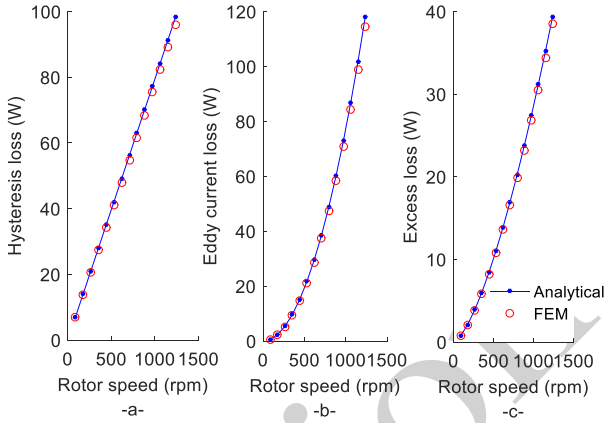

Fig. 20. On-load analytically and FEM predicted iron losses: **(a)** Hysteresis, **(b)** Eddy-current, and **(c)** Excess loss.

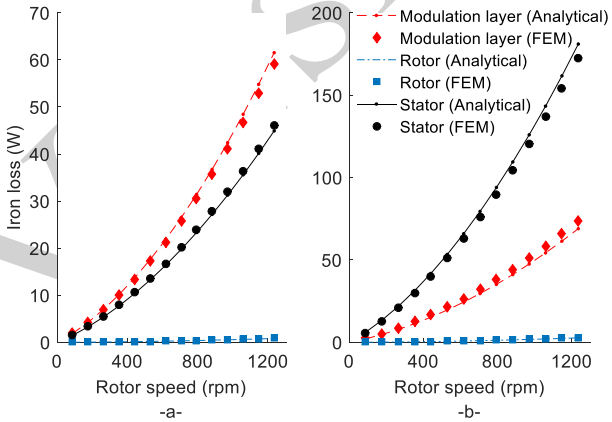

Fig. 21. Iron loss evolution in the various ferromagnetic parts (modulation layer, rotor and stator) at **(a)** no-load and **(b)** on-load condition.

In **Fig. 21(a)** and **(b)**, the iron loss evolutions in the modulation layer, rotor and stator according to rotor speed in both conditions (i.e., no-load and on-load of armature reaction field) are illustrated, respectively. As expected, in the no-load condition the iron losses are higher in the modulation layer than in the stator and very small in the rotor. However, in the on-load condition one can observe that the iron losses in the stator are increased and in the other (i.e., rotor and modulation layer), the iron losses are not much affected. The comparison between the proposed analytical model and FEM show a good agreement in the no-load condition [see **Fig. 21**].

The iron core losses in the FM-PMSM are shown in **Fig. 22(a)** according to supply stator current windings with three rotor speed (viz., 176, 617 and 1,235 rpm), and in **Fig. 22(b)** according to the rotor speed with three different supply current (viz., 0, 8, and 16 A). A good agreement can be see between the linear analytically obtained and the linear FEA results. In the nonlinear FEM can see a little error in the iron core losses compared to the two linear models results with 6.4 % and 5.2 % at 1,235 rpm and 16 A for linear analytical model and linear FEM respectively [see **Fig. 21**]. However, the error is very small especially if we take into consideration, the small calculation time taken by the linear models compared to the calculation time taken by the nonlinear FEM [see **Table II**].

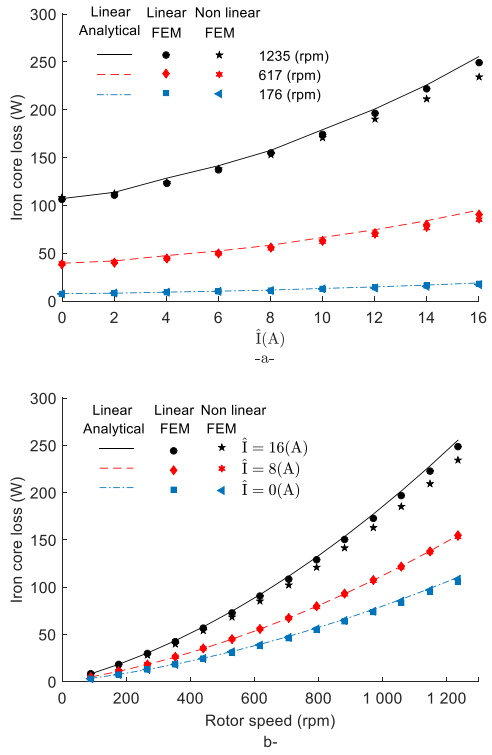

Fig. 22. Iron core loss evolution **(a)** function of the supply current and **(b)** function of the rotor speed.

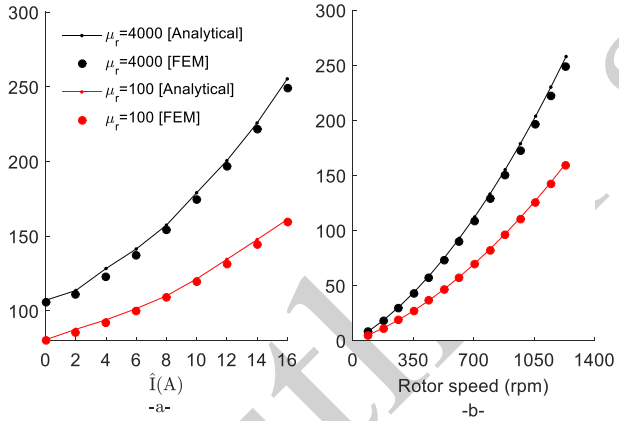

Fig. 23. Iron core loss evolution function of **(a)** the supply current at 176 rpm rotor speed and **(b)** function of the rotor speed at on-load condition with two different permeability values.

The iron core losses for two different values of the iron core relative permeability (viz., 100 and 4,000) are shown in **Fig. 23**. It can be observed that when the iron permeability is low then the iron core losses are low. However, in this case, the power provided by the machine are also low, compared to the case where the iron permeability is high.

VIII. Conclusion

In the presented paper, an analytical approach is proposed for calculation of iron core losses in FM-PMSMs under load and no-load conditions. This method is based on the analytical calculation of the iron magnetic field distribution taking into account of the permeability in the iron parts. It is based on the Maxwell-Fourier method (viz. the multi-layer model) and Cauchy's product theorem. The FM-PMSM is divided into eight regions and standard boundary conditions are used to solve the Poisson's and Laplace's equations. The magnetic field distribution in all regions of machine are predicted.

According to Bertotti's model, and taking into account the minor hysteresis loops and the DC bias flux density, the FVL method are used in the post-processing procedure to product the iron losses in the different parts of machine. The results showed that the analytical method give satisfactory results with FEM, which confirms the validity of the proposed model. It can be noted that the iron core losses are affected by the increase in the supply current and/or rotor speed as the results showed.

The next step will be extended to calculate the other losses, energy balance sheet and electromagnetic performances of this machine to be used in optimization procedures, in order to start making the proceeding to fabrication and manufacture of FM-PMSM for wind power applications.

Appendix

The stator current densities of slots for two tangential parts for three-phases current are defined as

$$J_{i,1} = \frac{N_c}{S}\mathbf{C}_{(1)}^T[i_a \;\; i_b \;\; i_c] \tag{A.1}$$

$$J_{i,2} = \frac{N_c}{S}\mathbf{C}_{(2)}^T[i_a \;\; i_b \;\; i_c] \tag{A.2}$$

where $\{i_a;\, i_b;\, i_c\}$ are the armature currents of three-phases, N_c is conductor number of slot coil, $S = \theta_s(R_3^2 - R_2^2)/4$ is the surface of the stator slot coil in kth region, and $\mathbf{C}_{(1)}^T$ & $\mathbf{C}_{(2)}^T$ are the transpose of the connection matrix linking the three-phases and the stator slots that represent the distribution of stator windings in the slots. The connection matrices $\mathbf{C}_{(1)}$ & $\mathbf{C}_{(2)}$ are given by

$$\mathbf{C}_{(1)} = [\mathbf{CC} + |\mathbf{CC}|]/2 \tag{A.3}$$

$$\mathbf{C}_{(2)} = [\mathbf{CC} - |\mathbf{CC}|]/2 \tag{A.4}$$

$$\mathbf{CC} = [\mathbf{C}\;\mathbf{C}\;\mathbf{C}\;\mathbf{C}] \tag{A.5}$$

$$\mathbf{C} = \begin{bmatrix} 1 & 0 & -1 \\ 0 & -1 & 1 \\ -1 & 1 & 0 \end{bmatrix} \tag{A.6}$$

These connection matrices can be generated automatically by using ANFRACTUS TOOL developed in **[29]**.

References

[1] L. L. Wang, J. X. Shen, P. C. K. Luk, W. Z. Fei, C. F. Wang, and H. Hao, "Development of a magnetic-geared permanent-magnet brushless motor," *IEEE Trans. Magn.*, vol. 45, no. 10, pp. 4578-4581, Oct. 2009.

[2] X. Zhang, X. Liu, and Z. Chen, "Analytical calculation of the magnetic field distribution in a flux-modulated permanent-magnet brushless motor," *in Proc. ICEMS*, Pattaya City, Thailand, Oct. 25-28, 2015.

[3] X. Zhang, X. Liu, J. Liu, and Z. Chen, "Analytical investigation on the power factor of a flux-modulated permanent-magnet synchronous machine," *IEEE Trans. Magn.*, vol. 51, no. 11, Nov. 2015, Art. ID 8110704.

[4] L. Jian, S. Member, K. T. Chau, and S. Member, "A coaxial magnetic gear with halbach permanent-magnet arrays," *IEEE Trans. Energy Convers.*, vol. 25, no. 2, pp. 319-328, Jun. 2010.

[5] M. Fratila, A. Benabou, A. Tounzi, and M. Dessoude, "Calculation of iron losses in solid rotor induction machine using fem," *IEEE Trans. Magn.*, vol. 50, no. 2, Feb. 2014, Art. ID 7020404.
[6] M. Fratila, A. Benabou, A. Tounzi, and M. Dessoude, "Iron loss calculation in a synchronous generator using finite element analysis," *IEEE Trans. Energy Convers.*, vol. 32, no 2, pp. 640-648, Jan. 2017.
[7] G. Bertotti, "General properties of power losses in soft ferromagnetic materials," *IEEE Trans. Magn.*, vol. 24, no. 1, pp. 621-630, Jan. 1988.
[8] Y. Huang, J. Dong, J. Zhu, and Y. Guo, "Core loss modeling for permanent-magnet motor based on flux variation locus and finite-element method," *IEEE Trans. Magn.*, vol. 48, no 2, pp. 1023-1026, Feb. 2012.
[9] C. Simao, N. Sadowski, N. J. Batistela, and J. P. A. Bastos, "Evaluation of hysteresis losses in iron sheets under DC-biased inductions," IEEE Trans. Magn., vol. 45, no. 3, pp. 1158-1161, Mar. 2009.
[10] Z. Zhang, L. Yu, L. Sun, L. Qian, and X. Huang, "Iron loss analysis of doubly salient brushless DC generators," *IEEE Trans. Ind. Elec.*, vol. 62, no 4, pp. 2156-2163, Apr 2017.
[11] L. Chen, H. Chen, and W Yan, "A fast iron loss calculation model for switched reluctance motors," *IET Elect. Power Appl.* vol. 11, no. 3, pp. 478-486, Mar. 2017.
[12] S. Xue, J. Feng, S. Guo, Z. Chen, J. Peng, W. Q. Chu,L. R. Huang, and Z. Q. Zhu, "Evaluation of hysteresis losses in iron sheets under dc-biased inductions," *IEEE Trans. Magn.*, vol. 53, no. 11, Nov. 2017, Art. ID 6100804.
[13] B. Sheikh-Ghalavand, S. Vaez-Zadeh, and A. H. Isfahani, "An improved magnetic equivalent circuit model for iron-core linear permanent-magnet synchronous motors," *IEEE Trans. Magn*., vol. 46, no. 1, pp. 112-120, Jan. 2010.
[14] A.R. Tariq, C.E. Nino-Baron, and E.G. Strangas, "Iron and magnet losses and torque calculation of interior permanent magnet synchronous machines using magnetic equivalent circuit," *IEEE Trans. Magn.*, vol. 46, no. 12, pp. 4073-4080, Dec. 2010.
[15] O. Messal, F. Dubas, R. Benlamine, A. Kedous-Lebouc, C. Chillet, and C. Espanet, "Iron losses in electromagnetic devices: Nonlinear adaptive MEC & dynamic hysteresis model," *Preprints "Automotive engineering"*, 2017010131, Jan. 2017, DOI: 10.20944/preprints201701.0131.v1.
[16] Z. Tian, C. Zhang, and S. Zhang, "Analytical calculation of magnetic field distribution and stator iron losses for surface-mounted permanent magnet synchronous machines," *Energies*, vol. 10, no. 3, p. 320, Mar. 2017.
[17] P. Liang, F. Chai, L. Chen, and Y. Wang, "Analytical prediction of no-load stator iron losses in spoke-type permanent magnet synchronous machines," *IEEE Trans. Energy Convers.*, vol. 33, no. 1, pp. 252-259, Mar. 2018.
[18] M. Desvaux, B. Multon, S. Sire, and H. Ben Ahmed, "Analytical iron loss model for the optimization of magnetic gear," in *Proc. IEMDC*, Miami, Florida, United States, May 21-24, 2017.
[19] R.L.J. Sprangers, J.J.H. Paulides, B.L.J. Gysen, and E.A. Lomonova "Magnetic saturation in semi-analytical harmonic modeling for electric machine analysis," *IEEE Trans. Magn.*, vol. 52, no. 2, Feb. 2016, Art. ID 8100410.
[20] Z. Djelloul-Khedda, K. Boughrara, F. Dubas, and R. Ibtiouen, "Nonlinear analytical prediction of magnetic field and electromagnetic performances in switched reluctance machines," *IEEE Trans. Magn.*, vol. 53, no. 7, Jul. 2017, Art. ID 8107311.
[21] R.L.J. Sprangers, J.J.H. Paulides, B.L.J. Gysen, J. Waarma, and E.A. Lomonova, "Semi-analytical framework for synchronous reluctance motor analysis including finite soft-magnetic material permeability," *IEEE Trans. Magne.*, vol. 51, no. 11, Nov. 2015, Art. ID 8110504.
[22] K. Ramakrishnan, M. Curti, D. Zarko, G. Mastinu, J.J.H. Paulides, and E.A. Lomonova, "Comparative analysis of various methods for modelling surface permanent magnet machines," *IET Elect. Power Appl.* vol. 11, no. 4, pp. 540-547, Apr. 2017.
[23] Z. Djelloul-Khedda, K. Boughrara, F. Dubas, A. Kechroud, and B. Souleymen "Semi-analytical magnetic field predicting in many structures of permanent-magnet synchronous machines considering the iron permeability," *IEEE Trans. Magn.*, vol. 54, no. 7, Jul. 2018, Art. ID 8103921.
[24] F. Dubas, and K. Boughrara, "New scientific contribution on the 2-D subdomain technique in Cartesian coordinates: Taking into account of iron parts," *Math. Comput. Appl.*, vol. 22, no. 1, p. 17, Feb. 2017, DOI: 10.3390/mca22010017.
[25] F. Dubas, and K. Boughrara, "New scientific contribution on the 2-D subdomain technique in polar coordinates: Taking into account of iron parts," *Math. Comput. Appl.*, vol. 22, no. 4, p. 42, Oct. 2017, DOI: 10.3390/mca22040042.
[26] L. Roubache, K. Boughrara, F. Dubas, and R. Ibtiouen, "New subdomain technique for electromagnetic performances calculation in radial-flux electrical machines considering finite soft-magnetic material permeability," *IEEE Trans. Magn.*, vol. 54, no. 4, Apr. 2018, Art. ID 8103315.
[27] L. Roubache, K. Boughrara, F. Dubas, and R. Ibtiouen, "Semi-analytical modeling of spoke-type permanent-magnet machines considering the iron core relative permeability: Subdomain Technique and Taylor polynomial," *Prog. Electromagn. Res. B.*, vol. 77, pp. 85-101, Jul. 2017.
[28] D. Meeker. Finite Element Method Magnetics. Version 4.2 (25 Oct. 2015 Build). Accessed: Sep. 05, 2018. [Online]. Available: http://www.femm.info
[29] D. Ouamara, F. Dubas, M.N. Benallal, S-A. Randi, and C. Espanet, "Automatic winding generation using matrix representation - ANFRACTUS TOOL 1.0 -," *Acta Polytechnica*, vol. 58, no. 01, pp. 37-46, Mar. 2018, DOI: 10.14311/AP.2018.58.0037.
[30] J. Lavers, P. Biringer, and H. Hollitscher, "A simple method of estimating the minor loop hysteresis loss in thin laminations," IEEE Trans. Magn., vol. 14, pp. 386-388, Sep 1978.

Zakarya Djelloul khedda was born in Chlef, Algeria, in 1988. He received the B.Sc and the M.Sc degree from Hassiba Benbouali University, Chlef, Algeria, in 2009 and 2011 respectively; he is working towards his PhD degree at Djilali Bounaama University of Khemis miliana, Algeria.

He is currently with SONELGAZ Company, is a company responsible for the production, transmission and distribution of electricity and gas in Algeria. His interests include design, modeling, optimization and control of electrical machines.

Kamel Boughrara was born in Algiers, Algeria, in 1969. He received the Engineer Diploma from Ecole Nationale Polytechnique Algiers, Algeria, and the magister degree from the University of Sciences and Technology Houari Boumediene, Algiers, Algeria, in 1994 and 1997, respectively, and the Doctorat d'Etat (i.e., PhD) degree from Ecole Nationale Polytechnique, Algeria, in 2008.

He is currently a Professor at Ecole Nationale Polytechnique (ENP), Algeria, and the Director of the Laboratoire de Recherche en Electrotechnique (LRE-ENP). His interests include modeling and control of electrical machines.

Frédéric Dubas was born in Vesoul, France, in 1978. He received the M.Sc. degree and the Ph.D. degree from the "Université of Franche-Comté" (Besançon, France) in 2002 and 2006, respectively, with a focus on the design and the optimization of high-speed surface-mounted permanent-magnet (PM) synchronous motor for the drive of a fuel cell air-compressor.

From 2014 to 2016, he has been the Head of "Unconventional Thermal and Electrical Machines" Team. He is the Head of the "Electrical Actuators" group in the "Hybrid & Fuel Cell Systems, Electrical Machines (SHARPAC)" Team. He works with ALSTOM Transports (Ornans, France), and RENAULT Technocenter (Guyancourt, France), where he is involved in the modelling, design and optimization of electrical systems and, in particular, induction and PM synchronous (radial and/or axial flux) machines, creative problem solving, and electrical propulsion/traction. He is currently an Associate Professor with the Département ENERGIE, FEMTO-ST Institute affiliated to the CNRS and jointly with the "Université of Franche-Comté" (Besançon, France).

He has authored over 100 refereed publications and he holds a patent about the manufacturing of axial-flux PM machines with flux-focusing. Dr. Dubas received the Prize Paper Awards in the IEEE Conference Vehicle Power and Propulsion (VPPC) in 2005 as well as the Prize Presentation Awards in the 19th International Conference on Electrical Machines and Systems (ICEMS) in 2017.

Abdelhamid Kechroud was born in Chlef, Algeria 1982. He received his Electrical Engineering degree from University of Sciences and Technology Houari Boumediene, Algiers, Algeria, in 2005 and the M.Sc degree from Institut National Polytechnique de Grenoble, France, in 2006 and the Ph.D. degree at the Eindhoven University, Netherlands in 2010. He has worked for over the last 12 years in several industries ranging from energy, lithography and automotive focusing on electromagnetic actuation systems development.

Currently he is with Vanderlande industries as system architect in warehouse automation systems. He is a member of the International Council on Systems Engineering (INCOSE). His research interests are electromagnetic actuation systems modelling and design and model based systems engineering.

Abdelouahab Tikellaline was born in Chlef, Algeria, in 1990. He received the B.Sc and the M.Sc degree from University of Sciences and Technology Houari Boumediene, Algiers, Algeria, in 2011 and 2013 respectively; he is currently a PhD student in the LESI Laboratory at Djilali Bounaama University of Khemis miliana, Algeria. His interests include modeling and design of permanent magnet machines.